

Cavitation and spallation in liquid metal droplets produced by subpicosecond pulsed laser radiation

M. S. Krivokorytov,^{1,2} A. Yu. Vinokhodov,² Yu. V. Sidelnikov,^{1,2} V. M. Krivtsun,^{1,3} V. O. Kompanets,¹
A. A. Lash,³ K. N. Koshelev,^{1,2} and V. V. Medvedev^{1,4}

¹*Institute for Spectroscopy, RAS, Fizicheskaya Street, 5, Troitsk, Moscow, Russia*

²*EUV Labs, Sirenevy Boulevard, 1, Troitsk, Moscow, Russia*

³*RnD-ISAN, Promyshlennaya Street, 1A, Troitsk, Moscow, Russia*

⁴*ISTEQ B.V., High Tech Campus 84, Eindhoven, The Netherlands*

(Received 14 October 2016; published 17 March 2017)

The deformation and fragmentation of liquid metal microdroplets by intense subpicosecond Ti:sapphire laser pulses is experimentally studied with stroboscopic shadow photography. The experiments are performed at a peak intensity of 10^{14} W/cm² at the target's surface, which produces shock waves with pressures in the Mbar range. As a result of such a strong impact, the droplet is transformed into a complex-shaped hollow structure that undergoes asymmetrical expansion and eventually fragments. The hollow structure of the expanding target is explained by the effects of cavitation and spallation that follow the propagation of the laser-induced shock wave.

DOI: [10.1103/PhysRevE.95.031101](https://doi.org/10.1103/PhysRevE.95.031101)

I. INTRODUCTION

Laser-induced shock waves are widely used in experimental studies of the rupture and fragmentation of condensed matter. Experimental data for laser-induced shocks in solid materials are available for a rich variety of materials and experimental conditions [1–8]. For liquids, most of the experiments on laser-induced shock waves were performed for optically transparent substances, e.g., water or glycerol [9–18]. The negligible attenuation of visible light in such materials facilitates direct observation of the effects of liquid rupture. In contrast, experimental data for liquid metals are scarce [19,20]. Experiments with liquid metals are, technically, more sophisticated, due to the requirement to operate at elevated temperatures. However, an understanding of the response of liquid metals, subjected to high-power laser pulses, is crucial for applications, such as the optimization of liquid metal targets for laser-produced plasma sources that emit extreme ultraviolet (EUV) radiation for lithography [21–30].

This Rapid Communication describes experimental studies of the deformation and fragmentation of free-falling liquid metal microdroplets by Mbar-scale shock waves that were generated by high-intensity ultrashort laser pulses. As a result of such a high-intensity shock wave, the spherical droplet is transformed into a complex hollow structure which is composed of two spheroidal shells. In our interpretation, the observed evolution of the droplet shape results from cavitation and spallation phenomena that occur after the propagation of the shock wave and rarefaction wave through the body of the target. Laser irradiation of the front face of the spherical droplet generates a convergent hemispherical shock wave that focuses in the central region, causing cavitation. The shock wave continues to the rear face of the droplet, where it encounters a free surface. The reflection and transmission of the shock wave from the rear surface causes spallation. The results are compared with previously reported experiments on the fragmentation of water droplets with laser-generated shock waves [14].

II. EXPERIMENTAL SETUP

The experiments were performed on the droplets of a eutectic Sn-In alloy with 48%–52% mass stoichiometry. The

alloy was heated to 140 °C during experiments, well above the melting temperature of the alloy (119 °C), which is almost two times lower than that of pure tin and indium. A relatively low operating temperature allowed easier experimental conditions, keeping all the other physical properties (density, viscosity, and surface tension) of the alloy similar to those of pure tin. The alloy droplets had a diameter of 56 μm and were generated using a commercial dispenser MJ-SF-01 by Micro-Fab Technologies. The droplets (also referred to as targets) were irradiated by pulses from a mode-locked Ti:sapphire laser (Spectra Physics, $\lambda = 780\text{--}820$ nm, pulse duration $\tau_L = 0.8$ ps). During irradiation, the droplet is in free fall in a vacuum chamber with a residual gas pressure of $<10^{-4}$ mbar. The experiments were performed at a maximum achievable pulse energy of $E = 2.3$ mJ. To visualize the droplet dynamics, we used stroboscopic shadowgraphy by backlighting the object with 30-ns-long pulses from a diode laser IL30C at $\lambda_{bl} = 850$ nm. The shadow images were recorded using a long distance microscope and a CCD camera. More details on the experimental setup, droplet generation, synchronization, and diagnostics can be found in Ref. [31].

III. RESULTS

In the experiment we examine the evolution of the droplet shape after the laser pulse impact for a fixed set of pulse parameters. Figure 1 shows a series of side-view shadowgraphs showing the initial droplet and the resulting target shapes at different moments of time after impact from a laser pulse propagating from left to right. The shadowgraphs are made at the following experimental conditions: initial droplet diameter $d = 56$ μm, $E = 2.3$ mJ, $\tau_L = 0.8$ ps, focal spot diameter $D = 72$ μm ($1/e^2$). The bright white spot that is present on all shadowgraphs corresponds to light emission from the plasma generated by the laser pulse, and captured by the camera due to the long exposure. The series of shadowgraphs presented in Fig. 1 shows that the target undergoes a rapid asymmetric expansion, followed by fragmentation. The target deformation during the first stages is accompanied by material ejection from the part of the target surface that was exposed to laser radiation [see Figs. 1(b)–1(d)]. Material ejection is represented on the

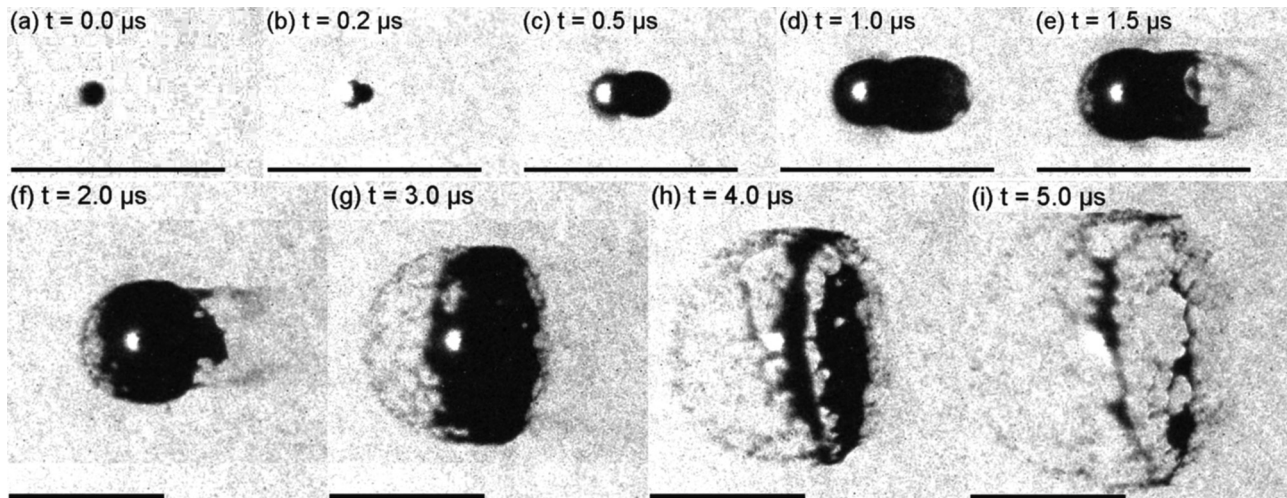


FIG. 1. The shadowgraphs of $56 \mu\text{m}$ droplets, taken at different time delays (t) after the 0.8 ps laser pulse; the scale bar on all shadowgraphs corresponds to $500 \mu\text{m}$.

shadowgraphs by the gray-to-black color gradient which can be interpreted as a dense vapor or a mist of microparticles.

The target deformation develops in the following way. The initial spherical droplet is transformed during the first microsecond into a complex shell-like structure [see Figs. 1(a)–1(d)], which can be approximated by two conjunct coaxial spheroids, as schematically shown in Fig. 2. Below, the part of the deformed target which expands around the initial droplet position is referred to as the front shell. Another part of the target, the elongated ellipsoidal part, is referred to as the rear shell. Later in the droplet's expansion, the deformed target fragments. The fragmentation first occurs on the rear side between 1.0 and $1.5 \mu\text{s}$, as depicted in Fig. 1(e). The rear part of the target completely fragments, i.e., its shadow image disappears between 2.0 and $3.0 \mu\text{s}$ [see Figs. 1(f) and 1(g)]. The front part of the deformed target fragments considerably slower. The fragmentation of the front part starts from the foremost point of the front part and propagates towards the position of constriction between the two parts of the target. As a result of the fragmentation, the residual target becomes ring shaped (in our interpretation), as is shown in Fig. 1(i). The deformation patterns were reproducible, allowing the analysis of the deformation dynamics as a function of strobe delay time, and the recording of explosion movies [32].

Now let us consider the process of the rear shell fragmentation in more detail. Figure 3(a) is a magnified image from Fig. 1(d) that corresponds to the target shape recorded at $1 \mu\text{s}$ after the laser pulse arrival. The yellow contour in Fig. 3(a) denotes the boundary of the target region that is opaque to the backlighting laser radiation. Beyond the yellow contour, in

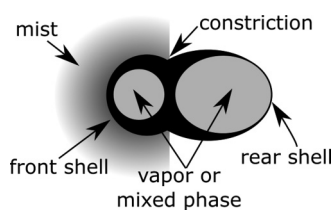


FIG. 2. Schematic representation of the laser-deformed target.

the region where fragmentation occurs, the rear shell becomes partially transparent, as can be seen from Fig. 3(a). Figure 3(b) shows the gray-level intensity curve, corresponding to the target opacity, which is plotted along the laser beam axis [see the corresponding red dashed line in Fig. 3(a)]. One can see from Figs. 3(a) and 3(b) that the opacity in the rear shell changes in a stepwise manner in the region of fragmentation [marked with vertical dashed lines in Fig. 3(b)]. This can be explained by the asymmetry in the fragmentation with respect to the direction of the laser irradiation. The observed transparency also indicates that the rear shell thickness does not significantly exceed the attenuation length for the wavelength of the backlighting laser radiation, i.e., the shell thickness in this region is on the scale of 10 nm .

Our experimental data also allowed quantitative estimates of the target expansion rate to be obtained. This was achieved

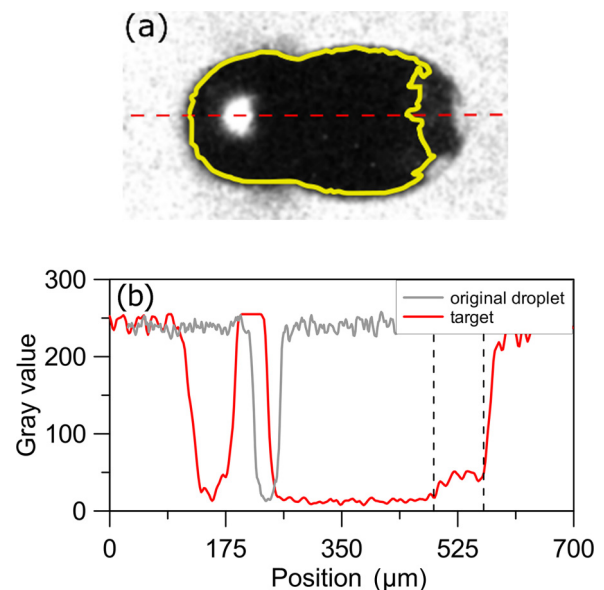


FIG. 3. (a) Shadowgraph taken at $1 \mu\text{s}$ after laser pulse; (b) gray-level intensity profile along the laser axis.

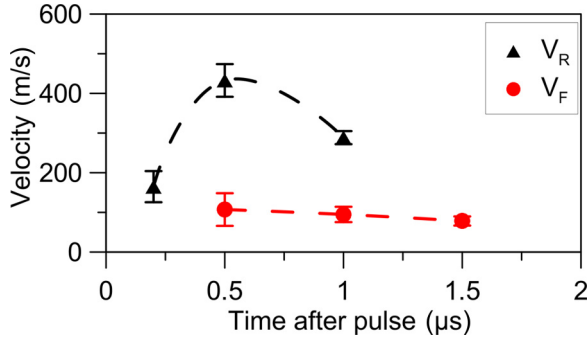


FIG. 4. Velocities of the target boundaries.

by calculating the displacement of the target's boundaries with respect to the boundaries of the initial target. For simplicity, we only quantify expansion along the laser beam axis by calculating the axial velocities of the front and rear part, v_r and v_f . Figure 4 shows the calculated velocity values versus time delay after the laser pulse impact.

Note that it is impossible to determine v_f values for delays shorter than 0.5 μs because of the plasma radiation captured by the camera [see Fig. 1(b)]. It is also impossible to determine v_r and v_f values for delays longer than 1.0 and 1.5 μs , respectively, because of the target fragmentation at the corresponding boundaries. The dashed curves on the graph are plotted to visualize the trends. From Fig. 4 it can be seen that the rear part of the target accelerates during the first 0.5 μs and then starts decelerating along with the front part.

IV. DISCUSSION

First, we discuss the regime of laser-matter interaction that corresponds to our experimental conditions. Metals are opaque for near-infrared radiation. At $\lambda \approx 800$ nm, the normal incidence reflection coefficients of tin and indium equal 89% and 83%, respectively [33,34]. The remaining incident laser energy, about 10%–15%, is absorbed within a thin near-surface layer. The layer thickness can be estimated using the radiation skin-depth formula $\delta = \lambda/(2\pi\kappa)$, with κ the extinction coefficient of the material at the given wavelength. Using tabulated optical constants, one obtains $\delta \approx 20$ nm for both metals. The laser pulse duration, $\tau_L = 0.8$ ps, is below the typical time scale for electron scattering on phonons in condensed matter. Hence, the laser energy is first absorbed by electrons, heating the electron subsystem. The energy exchange between the electron and ion subsystems occurs at the picosecond time scale. Note that the heat transport from the surface to the volume of the droplet is orders of magnitude slower. The thermal conductivity time in a droplet with diameter d can be estimated using the material's density ρ , heat capacity c , and thermal conductivity coefficient k as $\tau_{TC} = \rho c d^2/k$. For a tin droplet of 56 μm diameter, $\tau_{TC} \approx 85$ μs . Hence classical heat transport through the volume can be neglected, and the ion system is only heated within a thin near-surface layer of the droplet on the time scales that we consider. The maximal ion temperature can be estimated to be [35]

$$T_i \approx \frac{2I_a \tau_L}{\delta C_i}, \quad (1)$$

where I_a is the absorbed laser fluence, and C_i is the specific heat of the ion subsystem. For the given experimental conditions, T_i is about 10^7 K. This temperature significantly exceeds the values of critical temperature for tin ($T_c^{\text{Sn}} = 5809$ K) and for indium ($T_c^{\text{In}} = 6730$ K) [36]. Thus, our experimental conditions correspond to a regime of intense ablation of material from the laser-irradiated surface of the droplet. In turn, intense ablation leads to the formation of a plasma layer adjacent to the droplet surface. The plasma of the ablated material rapidly expands and, due to momentum conservation, an intense shock is imparted to the surface of the droplet. The intensity of this shock can be estimated with a commonly used scaling law relating laser fluence to plasma pressure, e.g. [14],

$$P(\text{Mbar}) = 0.4 \left(\frac{I_a (\text{TW}/\text{cm}^2)}{\lambda (\mu\text{m})} \right)^{2/3} \left(\frac{A}{2Z} \right)^{1/3}, \quad (2)$$

where A and Z are the atomic mass and number, respectively. Equation (2) gives pressures in the Mbar range for our experimental conditions. Rigorous hydrodynamic simulations for metal ablation by femtosecond laser pulses provide plasma pressure values of the same scale [37]. It is also important to note that the shock is applied to the droplet surface within a time that is significantly shorter than the sonic time scale, $\tau_s = d/v_s$. For a 56 μm droplet, the sonic time is approximately 30 ns, which is four orders of magnitude larger than the laser pulse length. Thus, the ultrashort, subsonic pressure kick of Mbar scale forms a shock wave in the laser-irradiated droplet.

The formation of the front shell of the expanding liquid structures shown in Fig. 1 can be explained by cavitation. In our experiments, the laser energy is deposited within a thin hemispherical layer on the droplet surface, and, as a result, a convergent hemispherical shock is formed. During the shock wave's propagation through the body of the droplet, the shock focuses at the central region due to its convergent geometry. The shock wave is followed by a rarefaction wave, which is also focused at the center of the droplet. The magnitude of negative pressure in the rarefaction region exerts a strain that exceeds the tensile strength of the material and thus causes the material to rupture.

We explain the formation of the rear shell in the expanding target as a result of an interaction of the shock wave with the rear surface of the droplet. When the incident shock wave is released at the rear surface, the compressed material expands freely, which produces another rarefaction wave. This rarefaction wave propagates backward to the front face, crossing the first rarefaction wave, which follows the initial shock wave. The superposition of these two rarefaction waves increases the dynamic tensile stress (magnitude of the negative pressure). If the magnitude of this stress exceeds the material's strength, a rupture occurs. This phenomenon has been studied over several decades in experiments with laser-induced shock waves in thick planar samples of solid materials. In such experiments, the dynamic rupture goes through a planar separation of a sample material, parallel to the shock-wave front. This phenomenon is usually referred to as spallation [38]. In experiments with laser-induced and explosion-induced shock waves in water, the rupture of liquid material was observed in the form of cavitation bubbles, produced due to shock release at the free surface. In 2016, Stan *et al.* observed spallation

in water microdroplets, produced by laser-induced expanding shock waves [14]. Similarly, in our experimental conditions, the release of the shock wave at the rear surface of the droplet produces a second cavity due to the effect of spallation.

Let us compare, in more detail, our experiments with those performed with water droplets by Stan *et al.* [14]. The latter used tightly focused femtosecond pulses from an x-ray free-electron laser. The laser beam was set to intersect the 55- μm -diam water droplets on their axis. Due to weak attenuation of the high-energy (8.5 keV) x rays in the target's body, the laser pulse energy was uniformly absorbed along a narrow (1 μm) filament. The absorbed laser energy was equivalent to filament pressures on the order of 1 Mbar. The high-pressure axial filament produced an expanding cylindrical shock wave in the droplet. The water transparency for visible light and the ultrafast optical imaging system allowed the authors to visualize the propagation of the shock-wave front with nanosecond time resolution. The shock-wave propagation was followed by the formation and expansion of a cylindrical cavity and the formation of a spall at the surface of the droplet. Contrary to that described by Stan *et al.*, our experimental conditions imply strong attenuation of the incident laser radiation in the target's material—the energy absorption occurs in a thin (~ 10 nm) surface layer of the irradiated hemisphere. Thus, the key qualitative difference between the two experiments is the geometry of the shock-wave propagation. However, the magnitudes of the shock waves and the targets' sizes are close in magnitude. For that reason, we conclude that the key phenomena that govern the process of the droplets' deformation are essentially similar.

Figure 5 schematically illustrates the shock-wave propagation through the body of the droplet and the main phenomena discussed above: (a) The ultrafast intense irradiation of a spherical droplet produces a hemispherical shock wave that converges towards the droplet center; (b) the shock wave is followed by a rarefaction wave, which also converges towards the center, providing high negative pressures, and, by these means, results in cavitation; (c) when passing the central region of the droplet, the shock wave expands; and (d) when reaching the rear face of the droplet, the shock wave produces a spall of a thin layer of the droplet material.

Thus, the dynamics and geometry of liquid expansion, which are observed in our experiments at the microsecond time scale, are governed by the spatial distribution of velocity in the shock-perturbed droplet, which is formed at a 10 ns time scale. It is also important to note that the propagation of intense shock waves induces phase transitions in materials. In our case, the dynamic processes of liquid metal fracture, including cavitation and spallation, can be considered to be a nonequilibrium phase transition through the formation,

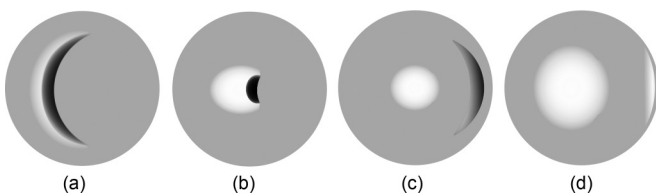


FIG. 5. Scheme of the shock-wave propagation through the droplet body.

growth, and coalescence of cavities, accompanied by material evaporation from the newly created surfaces. Since the shock-wave pressures are above or of the same scale as the critical pressure of the material, we expect the cavities to be filled with hot tin-indium vapor. The evolution of liquid shells filled with vapor generally depends on the balance between the vapor pressure inside the shell and the Laplace pressure. Low vapor pressure results in the collapse of cavitation. On the other hand, high vapor pressures result in the shell expanding, and the thinning of its walls until the surface breaks up or fragmentation occurs.

By using the measured values of the rear shell expansion velocity, it is possible to estimate the shock-wave pressure P_r when it reaches the rear face of the droplet. This can be done via the velocity doubling rule [38],

$$v_r = 2u = \frac{2P_r}{\rho v_s}, \quad (3)$$

where v_r is the speed of the body surface after the release of the shock wave at the free surface, u is the mass speed of matter behind the shock front, P_r is the pressure at the front of the shock wave, and ρ , v_s are the density and sound speed in the indium-tin alloy at 140 °C and 1 bar. Using the values for the velocity of the rear part from Fig. 3, $v_r \sim 100$ m/s and $v_s = 2000$ m/s, $\rho = 6.9$ g/cm³, one can roughly estimate the pressure at the shock-wave front as $P_r = \frac{1}{2}\rho v_r v_s \approx 7$ kbar. This simple estimation indicates that the shock-wave front pressure decreases by three orders of magnitude during its propagation through the droplet, and thus demonstrates strong dissipation of the shock-wave energy.

Using the measured data for shell expansion velocity in Fig. 3, it is possible to estimate the shell thickness values. To do so, let us consider the motion of an arbitrary small free-surface element. We denote the area of this element as S and its thickness h . The deceleration of this surface element can be calculated through the Laplace pressure ($P_L = 2\sigma/R$) as

$$a = -\frac{F}{m} = -\frac{2P_L}{\rho S h} = -\frac{4\sigma}{\rho h R}, \quad (4)$$

where σ is the density and surface tension of the liquid tin-indium alloy ($\sigma = 0.53$ N/m), R is the radius of surface curvature, and the factor 2 is due to the presence of two surfaces. At the same time, the value of deceleration can be determined from the experimental data from the slope of the curves in Fig. 2. Thus, having the measured values of a and R , one can estimate the front and rear shell thicknesses from Eq. (4). For the particular case given in Fig. 1(d), the curvature radii of the target parts are $R_r \approx R_f \approx 100$ μm and the deceleration values are $a_f = -3 \times 10^7$ m/s², $a_r \approx -3 \times 10^8$ m/s². These bring us to an estimate for the thicknesses: $h_r \approx 10$ nm, $h_f \approx 100$ nm. Note that this estimation for the rear shell thickness is close to our previous estimate using the shell transparency (Fig. 3).

V. CONCLUSION

We experimentally examined the deformation and fragmentation of a free-falling liquid In-Sn microdroplet, irradiated by a 0.8 ps laser pulse with an intensity of 10^{14} W/cm² at

the target's surface. According to well-known scaling laws, such intense irradiation results in Mbar-scale pressures in the laser-heated layer, and thus an ultrastrong shock wave with Mbar-scale pressure is formed. The shock wave has a convergent hemispherical geometry. As a result of the shock wave's propagation, the droplet undergoes a rapid asymmetric expansion and then transforms into a complex shape which could be interpreted as two conjunct hollow spheroid shells. The deformed liquid structures eventually fragmented. The hollow structure of the expanding target was explained by the effects of cavitation and spallation that follow propagation of the laser-induced shock wave. The experimental results

are of potential use for optimizing liquid metal targets for laser-produced plasma sources of extreme ultraviolet radiation, which are used in the next generation of lithography. Besides that, such experiments could be used for testing the numerical models of multiphase compressible flows in metals.

ACKNOWLEDGMENTS

We thank Chris Lee and Alexey Abrikosov for proofreading the manuscript. We also thank Mikhail Basko, Nail Inogamov, and Vasily Zhakhovsky for fruitful discussions.

-
- [1] S. Eliezer, I. Gilath, and T. Bar-Noy, Laser-induced spall in metals: Experiment and simulation, *J. Appl. Phys.* **67**, 715 (1990).
- [2] E. Moshe, S. Eliezer, Z. Henis, M. Werdiger, E. Dekel, Y. Horovitz, and S. Maman, Experimental measurements of the strength of metals approaching the theoretical limit predicted by the equation of state, *Appl. Phys. Lett.* **76**, 1555 (2000).
- [3] T. de Ressaiguier, S. Couturier, J. David, and G. Niérat, Spallation of metal targets subjected to intense laser shocks, *J. Appl. Phys.* **82**, 2617 (1997).
- [4] J. Ren, S. S. Orlov, and L. Hesselink, Rear surface spallation on single-crystal silicon in nanosecond laser micromachining, *J. Appl. Phys.* **97**, 104304 (2005).
- [5] G. Seisson *et al.*, Dynamic fragmentation of graphite under laser-driven shocks: Identification of four damage regimes, *Int. J. Impact Eng.* **91**, 68 (2016).
- [6] H. Tamura, T. Kohama, K. Kondo, and M. Yoshida, Femtosecond-laser-induced spallation in aluminum, *J. Appl. Phys.* **89**, 3520 (2001).
- [7] T. Kumada, T. Otobe, M. Nishikino, N. Hasegawa, and T. Hayashi, Dynamics of spallation during femtosecond laser ablation studied by time-resolved reflectivity with double pump pulses, *Appl. Phys. Lett.* **108**, 11102 (2016).
- [8] K. Sokolowski-Tinten, J. Bialkowski, A. Cavalleri, D. von der Linde, A. Oparin, J. Meyer-ter-Vehn, and S. I. Anisimov, Transient States of Matter during Short Pulse Laser Ablation, *Phys. Rev. Lett.* **81**, 224 (1998).
- [9] I. Akhatov *et al.*, Dynamics of laser-induced cavitation bubbles, *Exp. Therm. Fluid Sci.* **26**, 731 (2002).
- [10] O. Lindau and W. Lauterborn, Laser-produced cavitation—studied with 100 million frames per second, *AIP Conf. Proc.* **524**, 385 (2000).
- [11] K. Ando, A.-Q. Liu, and C.-D. Ohl, Homogeneous Nucleation in Water in Microfluidic Channels, *Phys. Rev. Lett.* **109**, 044501 (2012).
- [12] C. S. Peel, X. Fang, and S. R. Ahmad, Dynamics of laser-induced cavitation in liquid, *Appl. Phys. A* **103**, 1131 (2011).
- [13] C. A. Stan *et al.*, Liquid explosions induced by X-ray laser pulses, *Nat. Phys.* **12**, 966 (2016).
- [14] C. A. Stan *et al.*, Negative pressures and spallation in water drops subjected to nanosecond shock waves, *J. Phys. Chem. Lett.* **7**, 2055 (2016).
- [15] A. Lindinger *et al.*, Time-resolved explosion dynamics of H₂O droplets induced by femtosecond laser pulses, *Appl. Opt.* **43**, 5263 (2004).
- [16] S. Koch *et al.*, Time-resolved measurements of shock-induced cavitation bubbles in liquids, *Appl. Phys. B* **108**, 345 (2012).
- [17] S. R. Gonzalez Avila, P. Kerssens, J. Rapet, and C.-D. Ohl, Stereoscopic recording of droplet fragmentation, *Phys. Rev. Fluids* **1**, 50512 (2016).
- [18] S. R. Gonzalez Avila and C.-D. Ohl, Fragmentation of acoustically levitating droplets by laser-induced cavitation bubbles, *J. Fluid Mech.* **805**, 551 (2016).
- [19] S. I. Ashitkov, P. S. Komarov, A. V. Ovchinnikov, E. V. Struleva, and M. B. Agranat, Strength of liquid tin at extremely high strain rates under a femtosecond laser action, *JETP Lett.* **103**, 544 (2016).
- [20] T. de Ressaiguier, L. Signor, A. Dragon, P. Severin, and M. Boustie, Spallation in laser shock-loaded tin below and just above melting on release, *J. Appl. Phys.* **102**, 73535 (2007).
- [21] H. Matsukuma *et al.*, Correlation between laser absorption and radiation conversion efficiency in laser produced tin plasma, *Appl. Phys. Lett.* **107**, 121103 (2015).
- [22] H. Matsukuma *et al.*, Far-infrared-light shadowgraphy for high extraction efficiency of extreme ultraviolet light from a CO₂-laser-generated tin plasma, *Appl. Phys. Lett.* **109**, 051104 (2016).
- [23] D. Kurilovich *et al.*, Plasma Propulsion of a Metallic Microdroplet and its Deformation upon Laser Impact, *Phys. Rev. Appl.* **6**, 14018 (2016).
- [24] J. Fujimoto, T. Abe, S. Tanaka, T. Ohta, T. Hori, T. Yanagida, H. Nakarai, and H. Mizoguchi, Laser-produced plasma-based extreme-ultraviolet light source technology for high-volume manufacturing extreme-ultraviolet lithography, *J. Micro/Nanolith. MEMS MOEMS*, **11**, 021111 (2012).
- [25] I. V. Fomenkov, B. La Fontaine, D. Brown, I. Ahmad, P. Baumgart, N. R. Böwering, D. C. Brandt, A. N. Bykanov, S. De Dea, A. I. Ershov, N. R. Farrar, D. J. Golich, M. J. Lercel, D. W. Myers, C. Rajyaguru, S. N. Srivastava, Y. Tao, and G. O. Vaschenko, Development of stable extreme-ultraviolet sources for use in lithography exposure systems, *J. Micro/Nanolith. MEMS MOEMS*, **11**, 021110 (2012).
- [26] D. Hudgins, N. Gambino, B. Rollinger, and R. Abhari, Neutral cluster debris dynamics in droplet-based laser-produced plasma sources, *J. Phys. D: Appl. Phys.* **49**, 185205 (2016).
- [27] V. Y. Banine, K. N. Koshelev, and G. H. P. M. Swinkels, Physical processes in EUV sources for microlithography, *J. Phys. D: Appl. Phys.* **44**, 253001 (2011).
- [28] G. O'Sullivan, B. Li, R. D'Arcy, P. Dunne, P. Hayden, D. Kilbane, T. McCormack, H. Ohashi, F. O'Reilly, P. Sheridan, E.

- Sokell, C. Suzuki, and T. Higashiguchi, Spectroscopy of highly charged ions and its relevance to EUV and soft x-ray source development, *J. Phys. B: At. Mol. Opt. Phys.* **48**, 144025 (2015).
- [29] H. Gelderblom, H. Lhuissier, A. L. Klein, W. Bouwhuis, D. Lohse, E. Villermaux, and J. H. Snoeijer, Drop deformation by laser-pulse impact, *J. Fluid Mech.* **794**, 676 (2016).
- [30] A. L. Klein, W. Bouwhuis, C. Willem Visser, H. Lhuissier, C. Sun, J. H. Snoeijer, E. Villermaux, D. Lohse, and H. Gelderblom, Drop Shaping by Laser-Pulse Impact, *Phys. Rev. Appl.* **3**, 044018 (2015).
- [31] A. Yu. Vinokhodov, K. N. Koshelev, V. M. Krivtsun, M. S. Krivokorytov, Yu. V. Sidelnikov, V. V. Medvedev, V. O. Kompanets, A. A. Melnikov, and S. V. Chekalin, Formation of a fine-dispersed liquid-metal target under the action of femto- and picosecond laser pulses for a laser-plasma radiation source in the extreme ultraviolet range, *Quantum Electron.* **46**, 23 (2016).
- [32] See Supplemental Material at <http://link.aps.org/supplemental/10.1103/PhysRevE.95.031101> for different realizations of the droplet deformation at the constant strobe delay.
- [33] A. I. Golovashkin, I. S. Levchenko, G. P. Motulevich, and A. A. Shubin, Optical properties of indium, *JETP* **24**, 1093 (1967).
- [34] A. I. Golovashkin and G. P. Motulevich, Optical and electrical properties of tin, *JETP* **19**, 310 (1964).
- [35] B. N. Chichkov, C. Momma, S. Nolte, F. von Alvensleben, and A. Tünnermann, Femtosecond, picosecond and nanosecond laser ablation of solids, *Appl. Phys. A* **63**, 109 (1996).
- [36] A. L. Horvath, Critical temperature of elements and the periodic system, *J. Chem. Educ.* **50**, 335 (1973).
- [37] K. Eidmann, J. Meyer-ter-Vehn, T. Schlegel, and S. Hüller, Hydrodynamic simulation of subpicosecond laser interaction with solid-density matter, *Phys. Rev. E* **62**, 1202 (2000).
- [38] G. I. Kanel', V. E. Fortov, and S. V. Razorenov, Shock waves in condensed-state physics, *Phys.-Usp.* **50**, 771 (2007).